City Research Online

City, University of London Institutional Repository

In situ study of granular micromechanics in semi-solid carbon steels

J. Fonseca[a,b], C. O'Sullivan[b], T. Nagira[c], H. Yasuda[c], C.M. Gourlay[a]

[a] Department of Materials, Imperial College, London SW7 2AZ, UK

[b] Department of Civil and Environmental Engineering, Imperial College, London, SW7 2AZ, UK

[c] Department of Adaptive Machine Systems, Osaka University, 2-1 Yamadaoka, Suita, Osaka 565-0871, Japan

Abstract

The granular micromechanics of semi-solid steel at 80% solid are studied by synchrotron radiography. A particulate soil mechanics approach to image analysis shows that deformation occurs by the translation and rotation of quasi-rigid grains under the action of contact forces, and that the changes in directional fabric and grain–grain contacts occur by mechanisms similar to those of highly compacted soils including "locked sands". Grain-scale phenomena are then linked to the macroscopic displacement and strain fields and it is shown that shear-induced dilation is a fundamental response at both the grain and macro scales. Based on this, recommendations are made on future rheology experiments.

Keywords: Casting; Solidification; Synchrotron radiation; Granular materials; Soil mechanics

1   Introduction

Casting defects including hot tearing, shrinkage porosity and macrosegregation result from flow and deformation of the solid-liquid mixture during solidification [1]. In all casting processes, loads and pressure gradients act on the semi-solid due to solidification shrinkage, thermal contraction and gravity and in processes such as strip casting and semi-solid processing [2], deformation is applied externally by the process itself. For many decades, researchers have been building an understanding of semi-solid deformation with the aim of predicting and preventing casting defects and optimising casting processes [1, 3]. Research has shown that semi-solid deformation is complex, spanning from a Newtonian liquid through solid-liquid mixtures of increasing solid fraction to a polycrystalline viscoplastic solid.

It has been shown that semi-solid rheology is strongly dependent on the two-phase microstructure (solid fraction, morphology, and degree of cohesion) and the loading conditions (mode, accumulated strain and shear rate) [1, 4]. In the case of a globular morphology, semi-solid steels have been shown to be thixotropic [5] which has been attributed to the competition between agglomeration of globules with time and the break-down of agglomerates during shear [1, 6]. A range of other deformation mechanisms are also known to occur including viscoplastic deformation of the solid [4, 7, 8], fragmentation of the solid [7, 9], and "granular" phenomena associated with rearrangement of the solid as discrete bodies [9-13]. Furthermore, semi-solid deformation is not homogeneous at the micro-scale [12, 14, 15] and strain readily localises [11]. Due to this complexity and multiple simultaneous mechanisms, in the last 5 years various groups have developed techniques to directly observe the deformation mechanisms in situ and link the crystal-scale mechanisms to the macroscopic semi-solid response [13-18].

In situ synchrotron radiography studies of semi-solid deformation in Al-alloys [13] and steels [18] at 30-60% solid have confirmed the importance of interpreting the material response within a granular mechanics framework. Granular materials are disordered assemblies of macroscopic particles in contact [19] and include soils, powders, and cereal grain in silos. Under load, force is transmitted across the material via grain-grain contacts and a complex force chain network develops through the grain assembly. Consistent with this, radiography of equiaxed dendritic mush at ~30% solid and globular morphologies at 50-60% solid, deformed at 10^{-2} s^{-1}, has shown that grains rearrange as quasi-rigid bodies within an assembly of grains in contact [13, 18]. An important mechanical property in compacted granular materials is Reynolds' dilatancy [20], whereby the packing-density of densely packed grains decreases during shear. This occurs when the grains are sufficiently compacted that they push and lever each other apart as they rearrange under load [20, 21]. Recently, shear-induced dilation has been measured in macroscopic semi-solid deformation experiments on Al- and Mg- alloys [9, 11, 22] and crystals have been observed to push each other apart under load during synchrotron radiography of semi-solid Al- and Fe-alloys [13, 18]. These combined observations suggest that semi-solid alloys deform with fundamental similarities to granular materials such as water-saturated soils under certain combinations of microstructure and loading mode.

This paper examines the micromechanics of semi-solid steel at 70-90% solid within a soil mechanics framework and seeks to build a fundamental understanding of how force is transmitted through partially-solid alloys. Synchrotron radiography techniques from ref. [18] were developed further to directly image the microstructural response to load of semi-solid carbon steels at 70-90% solid. The focus of this paper is on 'fully-fed' high solid-fraction deformation in which liquid can flow into or out of the imaging field-of-view in response to any changes in solid packing-density. After qualitatively analysing deformation in 8 experiments, one sample that displayed behaviour representative of all 'fully fed' samples at 70-90% solid, was selected for a quantitative study of micromechanics in the sequence of radiographs. The approach quantifies the microstructural *fabric*, defined in soil mechanics as the arrangement of grains, grain groups and interstitial spaces [23]. This concept has proved useful in soil mechanics as two samples of the same granular material with similar solid fractions can exhibit a different mechanical response, depending on the grain orientations (e.g. [24]), and soil response is known to depend on the direction of loading relative to the particle and contact orientations (e.g. [25]). The analysis then focuses on (i) the evolution of grain-grain contacts during deformation, (ii) quantifying the displacement field, shear strain field and volumetric strain field, and (iii) comparing the overall response with soil behaviour.

2   Methods

2.1   Synchrotron radiography

Fe-2.08C-0.87Mn-0.45Si (mass%) high carbon steel was produced by melting pure elements and TiN powder in a vacuum-arc-melter. The Mn and Si contents were measured by ICP-AES and the C content was found using high-frequency combustion infrared absorption. The as-cast equiaxed-dendritic microstructure was then globularised by an extended semi-solid heat treatment of 100 hrs at 1250ºC (~70% solid) under Ar. This procedure produced an austenite grain size of ~350 μm and a nondendritic morphology. Specimens with dimensions of 10x10 mm x ~150 μm thickness were cut and polished from this feedstock, to produce an approximate monolayer of austenite grains in liquid on reheating.

The time-resolved X-ray imaging of semi-solid carbon steel has only recently become possible and the challenges associated with high temperature (1150-1540ºC) imaging of a

material consisting of γ-Fe and liquid phases with low absorption contrast are discussed in [26]. The experiments were performed on beamline BL20B2 at the SPring-8 synchrotron in Hyogo, Japan [27], building on techniques developed previously for steel [18, 26]. A 23 keV X-ray beam was used and the transmitted beam was converted to visible light by a scintillator and recorded by a 1000 x 856 pixel CCD chip at 5 frames per second and with 4.9 μm pixel size.
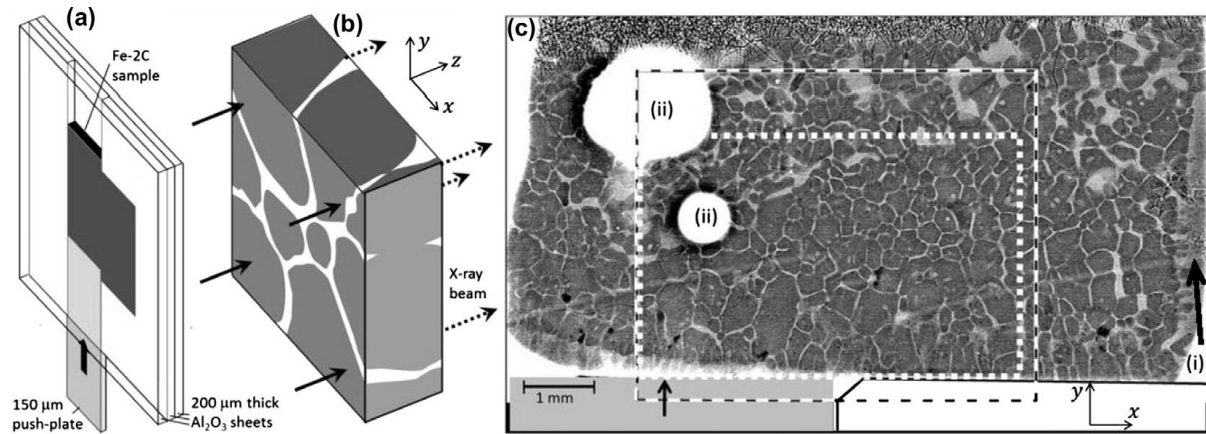

Figure 1: (a) Schematic of thin-sample shear-cell, with the z-direction exaggerated for clarity. (b) Magnified view of a small region of sample. (c) Bottom of the sample and shear cell prior to deformation (montage of six radiographs) with bounding walls and push-plate superimposed. The dashed box is the field of view during deformation, the smaller dotted box is the analysis region.

In situ semi-solid deformation was conducted in the thin-sample shear cell shown in Figure 1a, in which a push-plate penetrates into one half of the sample from below. Before an experiment, samples were partially remelted in the shear cell under a vacuum of 10^{-1} torr, and were held for ~10 min to thermally equilibrate the sample and cell. Isothermal deformation was then applied by a stepping motor with a displacement rate of 50 μm s^{-1}, corresponding to a global shear rate on the order of 10^{-3} s^{-1}. These boundary conditions have similarities to the direct-shear-box test used in soil mechanics [28] and in studies on the rheology of semi-solid Al alloys [29, 30]. Direct-shear and penetration configurations have been widely used, due to their experimental simplicity, in the testing of soils (e.g. [31]) and both 2D and 3D models of the direct shear test have been studied using the discrete element method (DEM) [32, 33]. The direct shear test is easier to carry out than a biaxial or triaxial test, but the stress and boundary conditions are more complex, complicating interpretation. However, it can capture dilatancy, stress-dependant stiffness and strength

4

and other important characteristics of soil response and so direct shear remains popular in both research and industry.

2.2 Image processing

Figure 1c is an image of the selected semi-solid sample prior to deformation, produced by stitching six radiographs together. The dashed box marks the field of view during real-time imaging and the smaller dotted box marks the analysis region studied in this paper. The analysis region has a region of lower packing density above and above right of it, and there is a "reservoir" of liquid at the right-hand edge of the sample (arrow i in Figure. 1c) that developed during partial remelting. Such liquid reservoirs are required to study "fully fed" high solid fraction deformation in which liquid can be drawn into or expelled from the interstitial spaces between the grains in the analysis region. Note that in radiography experiments at $g_s>0.8$ in which there were no liquid reservoirs, shear-induced dilation led to casting defects (surface sinks, pores and cracks). Defect formation in such "unfed" tests will be the focus of a separate publication. This paper considers only the case of "fully fed" ("drained" in soil mechanics terminology) high solid fraction deformation.

Figure 1c shows that the initial sample also contains two pores or surface sinks (arrows (ii)). Pores formed during remelting in some samples and did not alter the fundamental grain-level mechanisms being studied here. This sample was selected because there was no measurable change in sample thickness during loading nor any development of overlap between grains, indicating that grain rotations and translations are confined to the imaging plane and that deformation is well-approximated as quasi-2D.

The grain size is ~350μm and the sample is therefore ~0.5 as sketched in Figure 1b. Therefore, the analysis approach taken here is based on identifying the projected grains and the contact pixels between neighbouring grains (using a simple definition of a contact), and studying the changes in projected grains and contacts during loading.

A manual technique was used to identify the perimeter of the projected grains. Coordinates were selected 3-5 pixels apart along each apparent S-L interface using the Image J 'point picker' plugin (National Institute of Health, USA). The coordinates were imported into MATLAB (Mathworks, Natick, MA, USA) and an integer value was assigned to points belonging to each grain. The interface was approximated by a polyline connecting the

imported pixels and, using the MATLAB function poly2mask, a region of interest (ROI) was computed so that every grain was represented by a cloud of points (pixels) sharing a common integer value. The pixels located outside the S-L interfaces defined the liquid space and were attributed the value 0. Figures 2(a)-(b) summarise the image processing approach. Four stages during deformation were analysed, giving information on three increments of deformation.
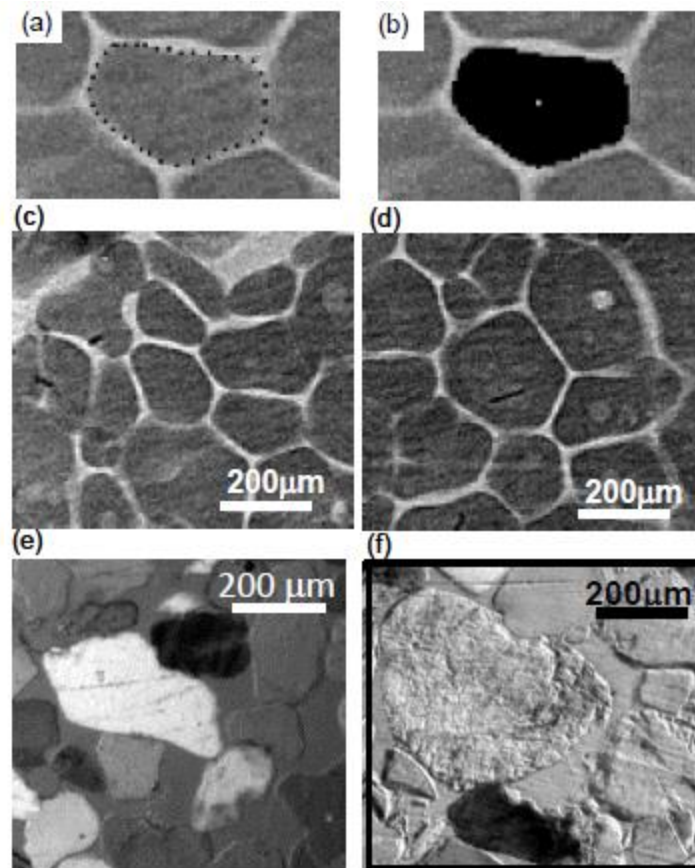

Figure 2: (a)-(b) Steps to segment and identify individual grains. (c)–(f) Images of microstructure of (c and d) the steel analysed in this project; (e)–(f) optical micrographs of a locked sand from Ref. [34].

3   RESULTS

3.1   Initial Microstructure

The sample consists of an austenite-liquid mixture with non-dendritic γ-Fe morphology and ~350µm grain size (Figure 1b). When considering the projected-area grains, the initial solid fraction in the imaging field of view is 88%. The true solid fraction will be somewhat lower. Typical regions of the microstructure are shown at higher magnification in Figure 2(c) and

6

(d). The 100hr semi-solid heat treatment produced non-dendritic γ-Fe grains with a small amount of entrapped liquid within some grains, as is typical of globularised microstructures [1]. Since the sample is at high solid fraction, the grain morphology is partially globular and partially polygonal. As a consequence, some S-L interfaces are concave to accommodate the convex S-L interfaces of neighbouring grains and the majority of interfaces are relatively straight.

This semi-solid steel microstructure shares striking similarities with a specific type of soil known as 'locked sand'. Figure 2(c) shows an optical image of a thin (30 μm) section of a locked sand (Reigate sand from Southeast England [34]) under cross-polarised light. The mean solid fraction in this sample is 70% [34]. As can be seen, most contacts are 'long-straight' and 'concavo-convex' using the terminology of [34, 35], with occasional interpenetrating contacts, similar to the semi-solid steel in Figure 2(a)-(b). Locked sands are geological old sand formations that have developed large contact areas between grains as the soil has been densified under overlying soil layers [36]. When locked sands are sheared, failure occurs at small strains (typically less than 0.1%) and is accompanied by extremely high rates of dilation of $-\dfrac{\delta \varepsilon_V}{\delta \varepsilon_S} > 1.8$, where ε_V is the volumetric strain and ε_S is the shear strain (e.g. [37]). Due to these similarities in the microstructure, the grain level behaviour of the semi-solid steel is compared with the behaviour of locked sands in the current study.

3.2   *Microstructural response to load*

The four stages of deformation studied correspond to pushing-plate displacements of 0 μm , 404 μm (1.2x d_{50}), 878 μm (2.5x d_{50}), and 1072 μm (3.1x d_{50}), where d_{50} is the median projected grain diameter (348 μm). The radiographs and segmented microstructures are shown for three of the four deformation stages in Figure 3. The segmented images contain 209 γ-Fe grains and the same grains are present at each stage. As the pushing-plate moves up, the smallest surface sink/pore is closed-in by the surrounding grains and the larger pore is pushed up, partially out of the field of view. From a detailed visual analysis of Figure 3, and a range of repeated experiments under similar conditions, the key features of deformation can be summarised as: (i) macroscopic shape change occurs by grain rearrangement coupled with interstitial liquid flow, (ii) most grains have translated and

7

rotated as discrete bodies under the action of the contact forces (here both normal and tangential components of contact forces will induce a moment on the non-spherical particles), (iii) individual grains do not seem to have been deformed, (iv) grain motion is localised in certain areas, producing inhomogeneous deformation, and (v) significant shear-induced dilation occurred, causing the overall solid fraction to decrease during rearrangement (compare Figure 3(f) and (d)). The dilation is accommodated by the in-flow of liquid from outside of the field of view. These deformation features are examined quantitatively in the remainder of the paper.
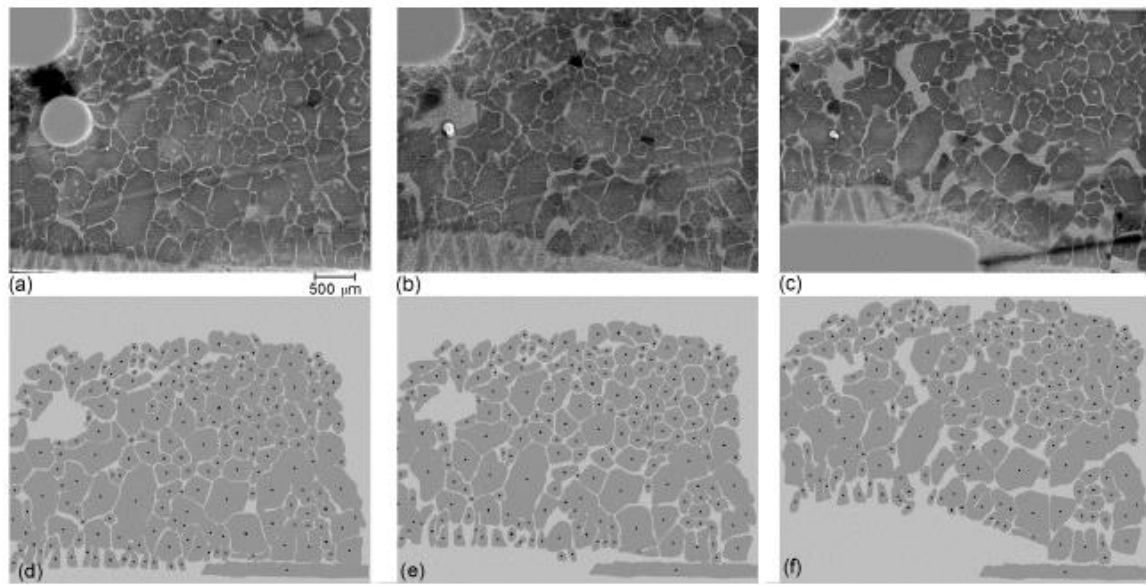

Figure 3: (Top row) Radiographs of deformation stages 1, 2 and 4. The images have been flattened to aid visualization. (Bottom row) The corresponding segmented images and grain centroids.

To examine whether there are significant changes in the projected-areas of the grains, the change in equivalent circle diameter was calculated for each projected grain and the data are plotted as a histogram in Figure 4(a). The mean absolute change in equivalent circle diameter is 1.2px. The image in Figure 4(e) shows that an apparent change in diameter of 1.2px can be attributed to the uncertainty in identifying the pixels of the perimeter of each projected grain, and gives a measure of the sensitivity and reproducibility of the analysis technique. Figure 4(a) indicates that there is no significant change in the projected-areas of the grains. Consistent with this, the mean change in diameter is only 0.24px, confirming that there is no significant melting, growth or fragmentation of the γ-Fe during the

experiment. Figure 4b shows that the γ-Fe grains have a median size of $d_{50} =348\mu m$, and the Reigate sand, the locked sand used for comparison here, has $d_{50} =325\mu m$.
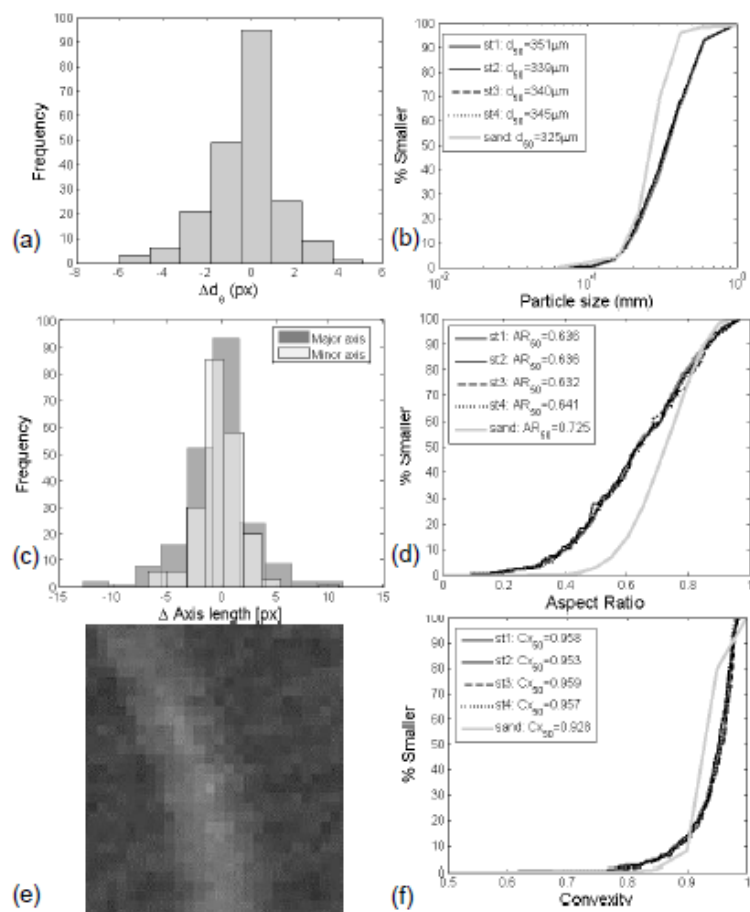

Figure 4: (a) Histogram of the change in equivalent circle diameter of the grains from stages 1 to 4. (b) Grain size distribution. (c) Histogram of the change in major and minor axes of grains from stages 1 to 4. (d) Aspect ratio distribution. (e) Pixel intensity at a typical solid–liquid interface. (f) Convexity distribution.

To assess whether the individual γFe grains were deformed as they rearranged, the shape of each grain was quantified by the aspect ratio (AR). The changes in major and minor axis lengths are shown for all grains as a histogram in Figure 4(c). The mean absolute change is 2.1px and 1.4px for the major and minor axes respectively. Comparing with the image in Figure 4(e), these changes can be attributed to uncertainties in selecting the pixels of the projected grain perimeter. An additional analysis of the change in grain dimensions at contacts is presented in the Supplementary Information (SI) and confirms that there is no significant deformation of the individual grains within the resolution of the experiment, and that the rearranging grains are well-approximated as quasi-rigid.

Two shape factors were used to quantify the shape of the projected-grains: the aspect ratio and the convexity (Cx), defined as the ratio between the area of the grain and the corresponding convex area. As would be expected for quasi-rigid grains no noticeable change in convexity during shearing was observed Figure 4(f). Comparing the grain shape distributions with the Reigate sand grains, Figure 4(d) and (f) show that AR values smaller than 0.5 were rarely observed in the sand, whereas the semi-solid contained a number of γ-Fe grains with AR values lower than 0.5. Additionally, the γFe grains have more convex geometries than the sand grains with a mean convexity value of 0.96.

In Figure 3, many grains rotate and translate relative to one another, implying that force is being transmitted across the contacts between grains and that there is limited cohesion between most grains. The individual displacements cause the distance between grain centroids and the shape and size of the contacts to vary. Next, these features are quantified to provide insights on force transmission through the two-phase microstructure and the origin of shear-induced dilation in partially-solid alloys.

Due to a pixel size of 4.9μm and radiographic imaging through a sample 0.43 median grain thick, we do not have access to information of the detailed shape and inclination of contacts. Therefore, a criterion for a contact was developed based on the change in X-ray intensity between neighbouring grains. As overviewed in the SI, two γFe grains are considered to be in contact if the region of apparent liquid between them is less than five pixels (24.5 μm) thick. This approach does not give information on the detailed shape/inclination/curvature of contacts nor on the extent of a contact in the thickness-direction. Instead it provides a reproducible definition of a contact pixel that is adequate for a quantitative study of contact evolution during shear.

In order to identify contact pixels in the segmented images, a morphological-dilation of the grains was applied in an image processing stage. Figure 5(a) shows a small region where each grain is represented by a different grey level. In Figure 5(b) the grains have been morphologically-dilated to fill the space between grains with solid pixels and identify the contacts. Similar to [34], for two contacting grains, contacts are identified by a forward pass, comparing pixel (x+1,y) with pixel (x,y), and a backward pass comparing pixels (x,y) with (x-

1,y). The results were merged to add data to the array of contact pixel coordinates for a given grain, such that if either sweep defines a pixel to be a contact, it remains a contact pixel no matter what the second sweep determines. This process was repeated along the y axis.
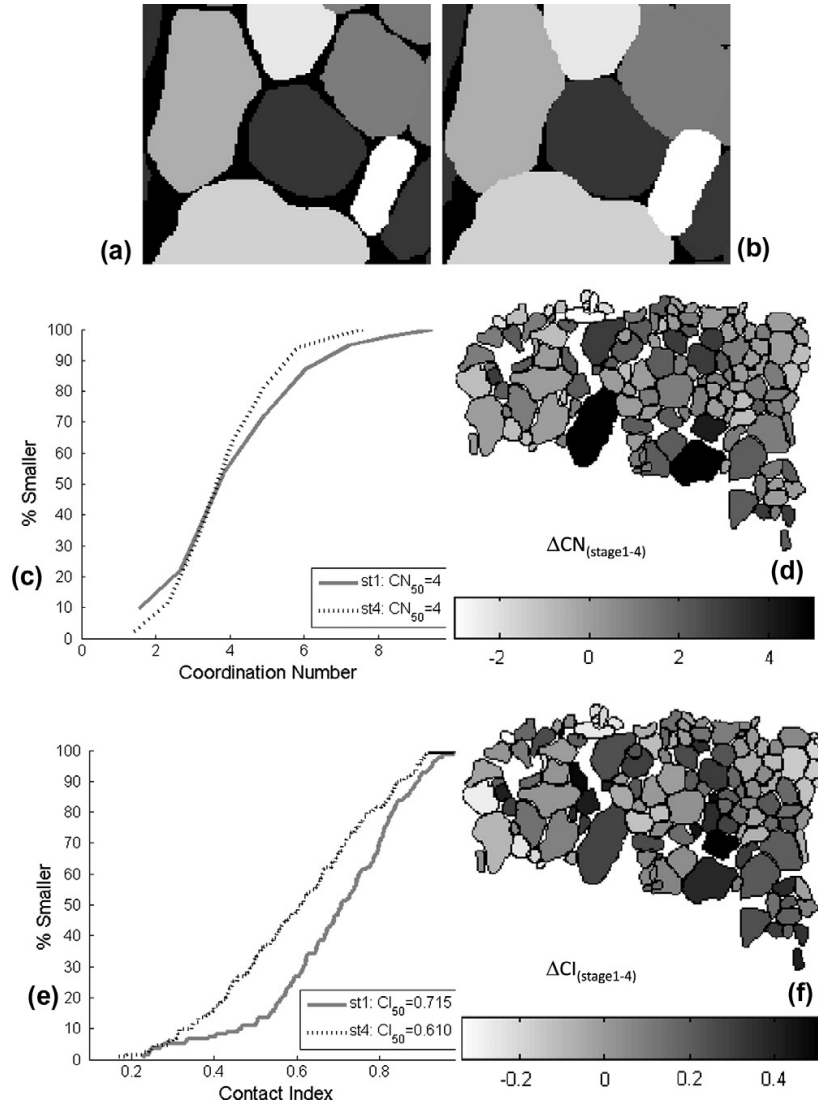

Figure 5: (a and b) Morphological dilation for contact detection: (a) original segmented image and (b) morphologically-dilated image. (c) Coordination number (CN) distribution and (d) change in CN for each grain. (e) Contact index (CI) distribution and (f) change in CI for each grain. A positive change is defined as loss.

For the study of contact evolution during deformation, changes in the coordination number, contact index and the length of doublet vectors were considered. The coordination number (CN) is defined as:

$$CN = \frac{2N_C}{N_P}$$

(1)

where N_P is the number of grains and N_C is the number of contacts which is multiplied by 2 as each contact is shared between two grains. Figure 5(c) shows the coordination number distributions (CND) for stages 1 and 4. There is no significant difference between the curves, with only a slight reduction in the incidence of the highest CN values, and the average values (CN_{50}) are the same for both stages. Figure 5(d) shows the change in CN for each grain between stages 1 and 4 by shading grains by the number of contacts gained or lost. Larger grains are, in general, associated with a greater loss of contacts (are darker). When grain size was plotted against the coordination number the linear correlation found, although weak for both stages, was much greater for the initial stage (R^2=0.55) than for stage 4 (R^2=0.25). This shows that the larger grains tend to have more contacts as is expected for a dense granular material. However, when rearrangement occurs, the loss of contacts is also a function of the grain location in relation to regions of localised dilation. Figure 5(d) confirms that many grains see no variation in CN and that dilation occurs in localised regions.

The CN does not consider contact size and gives contacts with a finite projected-length the same weight as point contacts. In contrast, the contact index is the fraction of perimeter pixels that are contact pixels and is defined as [34, 36]:

$$CI = \frac{1}{N_P} \sum_{i=1}^{N_p} \frac{1}{Sp_i} \sum_{j=1}^{Nc,i} Sc_j$$

(2)

where N_P is the number of grains in the assembly, Sp_i is the perimeter of grain i, Sc_j is the length of the contact j and $N_{c,i}$ is the number of contacts involving grain i. Figure 5(e) shows the contact index distribution (CID) for stages 1 and 4. In comparison with the CND curves the CID curves are clearly distinct at stages 1 and 4, with average contact index values (CI_{50}) decreasing from 0.715 to 0.610 from stage 1 to 4. That is to say, there is a decrease in the projected length of contacts during shearing, consistent with the images in Figure 3. As previously observed for a locked sand [34], the results demonstrate that, when dealing with grains that form contacts with a finite size (projected-length) rather than point contacts, the

change in CI captures more information on the evolution of contacts during rearrangement than the change in CN. Figure 5(f) shows that grains with a greater reduction in contact size (darker grains) are generally located in the regions of greater dilation and they are not necessarily the grains with the greatest change in CN in Figure 5(d). The value of measuring both the change in CN and CI in understanding shear-induced dilation is considered further in the SI.

Contact evolution was also studied by quantifying the change in doublet vectors during deformation. As shown in Figure 6(a), the doublet vector is the line between neighbouring centroids and does not consider whether adjacent grains are in contact [38]. This is in contrast to the branch vector which is the line joining the centroids of contacting grains. In Figure 6(b) the network of doublet vectors is superposed on the image of the grain system, where the line thickness is proportional to the increase in doublet vector length between stages 1 and 4. The larger displacements (thicker lines) are located in the regions of greater local dilation and naturally these regions coincide with the region experiencing the greatest reduction in the number of contacts per grain (Figures 5 (d) and (f)). Local contraction, represented by dashed lines, was observed only for a few grains, in general affected by the closing-in of the small surface sink/pore.
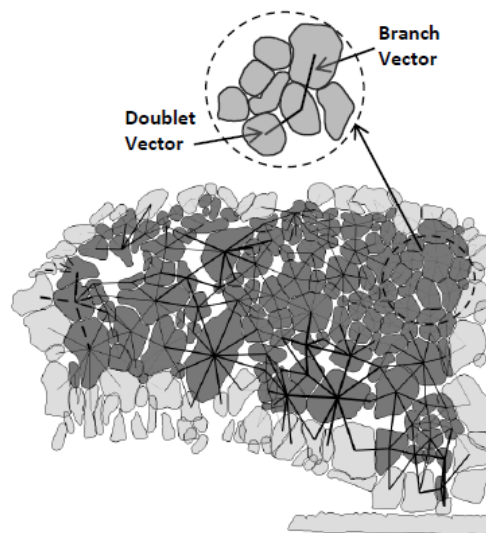

Figure 6: (a) Definition of the doublet and branch vectors. (b) Change in the branch vector length between stages 1 and 4. Solid lines are increase in branch vector length, dashed lines are decrease, and the lines thickness indicates the magnitude of the change.

The directional fabric was quantified using the orientation of the grains and contacts following micro-mechanics studies on granular materials [39]. The vector describing the major axis orientation of grains was obtained by applying principal component analysis (PCA) [40] to the cloud of points defining each grain, and grain rotation was measured from the change in major axis during shear. PCA was found to be inaccurate for the smallest and most circular grains where a small error in defining the shape of a grain can affect the location of the major axis. Therefore, an additional analysis (overviewed in the SI) was conducted to check and optimise the measured rotations.

Figure 7(a) gives examples of the orientation vector of the major axis of a grain. The rotation field between stages 1 and 4 is presented in Figure 7(c) where each grain has been shaded by the rotation of its major axis in degrees. Comparing Figure 6(b) with Figure 7(c) some correlation can be seen: regions where grains rotate more (Figure 7(c)) generally correspond to regions with greatest increase in doublet vector (thicker lines in Figure 6(b)), which correspond to regions of greatest local dilation. This highlights the role of rotation in shear-induced dilation: rearrangement causes grain rotation and the rotation of non-spherical grains in a compacted granular assembly creates interstitial space. The link between particle rotations and regions of higher dilation has previously been shown in discrete element method simulations of granular materials, e.g. [28].
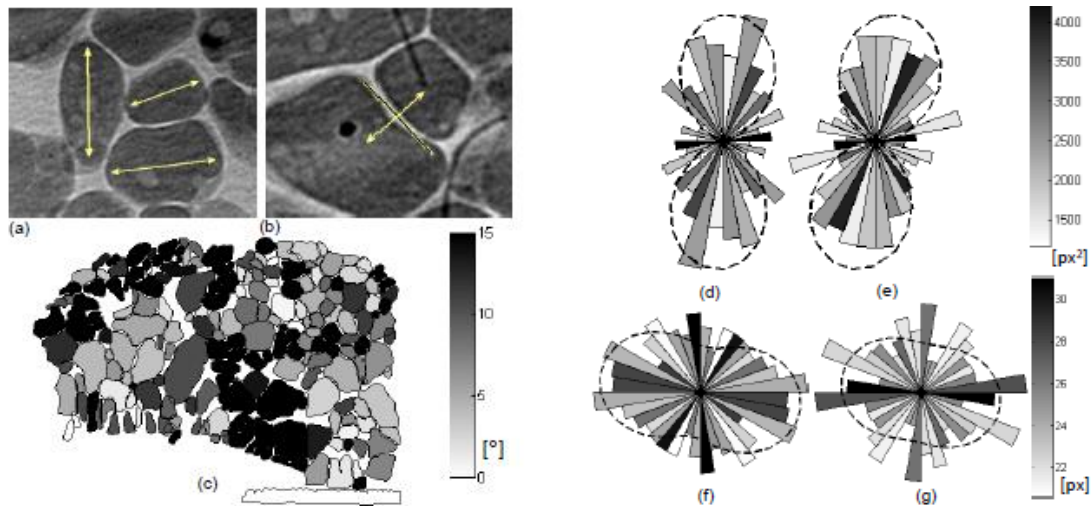

Figure 7: (a)-(b)Vectors representing (a) the grain orientation and (b) the contact normal orientation. (c) Rotation field between stages 1 and 4. (d)-(e) Rose diagrams of the particle orientation for (d) stage 1 and (e) stage 4, and contact normal orientation for (f) stage 1 and (g) stage 4.

Polar histograms (rose diagrams) of the major axis orientations are shown in Figures 7(d) and (e) for stages 1 and 4 respectively. The shading assigned to each histogram bin is proportional to the average size of the grains (area in px^2) with orientations within the bin limits.   Prior to deformation (stage 1) the grains are predominantly oriented along the vertical direction, with a dominant orientation of 86° to the horizontal (as calculated from eigenvalue analysis of the fabric tensor). As shearing progresses the grains rotate clockwise and the orientation of the major eigenvector is 86, 83, 78 and 79° to the horizontal for the four deformation stages respectively. The small number of grains (209) does not allow conclusions to be drawn regarding the effect of grain size on the change of grain orientation.

Further insights into load transmission were obtained by considering the change in orientation of contact normals, defined as the vector orthogonal to the contact between two grains (Figure 7(b)) [39]. Figures 7(f) and (g) show the distribution of contact normals where bins are shaded by the length of the contacts (in pixels) with that orientation. For the initial stage the contact normals are predominately orientated along the horizontal direction (with a predominant orientation of 12° to the horizontal). As shearing progress, the predominant orientation rotates slightly clockwise. This is in agreement with the overall rotation of the grains, i.e. as the grains become less vertical the contact normal becomes less horizontal. The distribution of contact normals becomes more isotropic from stage 1 to stage 4. This appears to be a shift of the larger contacts from vertical to more horizontal positions as shearing progresses, but this observation is limited by the small number of contacts in the field of view.

3.3   *Macroscopic response to load*

To quantify the macroscopic shear-induced dilation, a region containing 135 grains was selected that excludes grains which were affected by gravity (at the bottom-right of the sample) or by the surface sinks/pores. The projected-area of this region was measured by connecting the centroids of the outer grains as shown for stages 1 and 4 in Figure 8(a) and (b) respectively. Figure 8(c) is a plot of the volumetric strain versus the deviatoric strain (i.e. difference between major principal strains) calculated relative to the initial geometry in Figure 8(a) for the three subsequent deformation stages. The strains were calculated from the entire set of grain displacements using the best fit approach described in [41]. Positive

volumetric strains indicate dilation. When the overall response is considered in this way, the grain-assembly clearly dilates continually during shear deformation (indicated by the deviatoric strain values) and no steady-state volumetric strain is reached in this experiment.
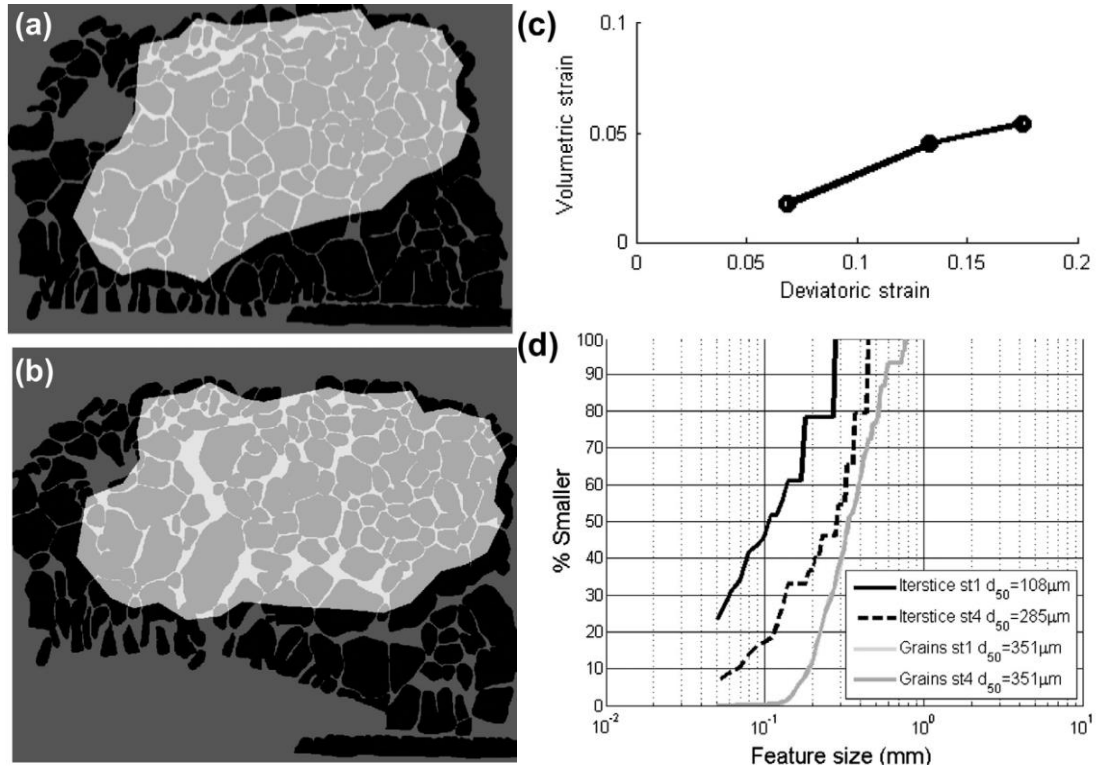

Figure 8: Dilatancy analysis. (a) Initial region (b) Final region. (c) Plot of volumetric strain against deviatoric strain. (d) Size distribution of liquid-filled interstices and grains at stages 1 and 4.

The dilation was also quantified by analysing the change in size of the liquid-filled interstices. Using the morphologically-dilated images from Figure 5, the interstices form isolated regions and the size of each can be expressed as an equivalent circle diameter. The size of the interstices is plotted as a distribution of equivalent circle diameters in Figure 8(d). For load stage 1 the mean diameter of the spaces is much less than the mean diameter of the grains, d_{50}^{liquid}= 108µm versus d_{50}^{grains} = 351 ±10 µm. By loading stage 4, the spaces increase considerably in size to d_{50}^{liquid}= 285µm versus d_{50}^{grains} = 345 ±10 µm.

The displacements of the grain centroids were used to link the grain-scale behaviour to the macroscopic deformation. Figure 9(a) shows the centroid displacement field between stages 1 and 2, superposed on the average image of the 85 frames between stages 1 and 2. The general form of the displacement field is similar to past work on semi-solid Al-15Cu and

16

Fe-2C subjected to the same loading mode and a similar deformation increment but at lower solid fraction [13, 18]: grains are pushed upward ahead of the plate and develop a flow to the right, away from the plane of the advancing plate. The orientation of the displacement vectors in Figure 9(a) correlate well with the clockwise change in predominant particle orientation vector during shearing in Figure 7(d)-(e).
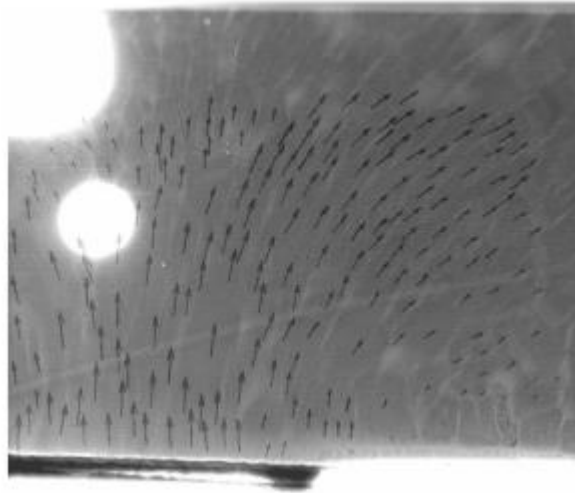

Figure 9: Displacement field between stages 1 and 2 superimposed on the time-average image of the 85 frames between stage 1 and 2

Figure 8(c) considered the average, overall strains. The strain fields were also calculated by triangulating the grain centroids and then using the centroid displacements with the constant strain triangle shape functions used in finite element analysis to calculate a strain for each triangle defined by a triad of three centroids (e.g. [42]). Figure 10(a) shows the Delaunay triangulation used for the strain analysis, obtained using the built-in MATLAB function **delaunay**. This approach yields the strain tensor, and the volumetric strain was found from the trace of the tensor. The volumetric strain field was visualised by shading each triangle according to the change in projected-area, and the shaded regions were smoothed and the bottom truncated in order to obtain a more elucidative figure as presented in Figure 10(b). The darkest regions correspond to a dilation of 0.3 (30% increase in triangle area). The lightest regions (associated with compaction) represent regions where the solid fraction increases. The deviatoric strain field is presented in Figure 10(c), where the shear strains are taken as the difference between the eigenvalues of the strain tensor (i.e. the principal strain differences). The darker regions correspond to areas of higher shear strains (greater than 0.8).
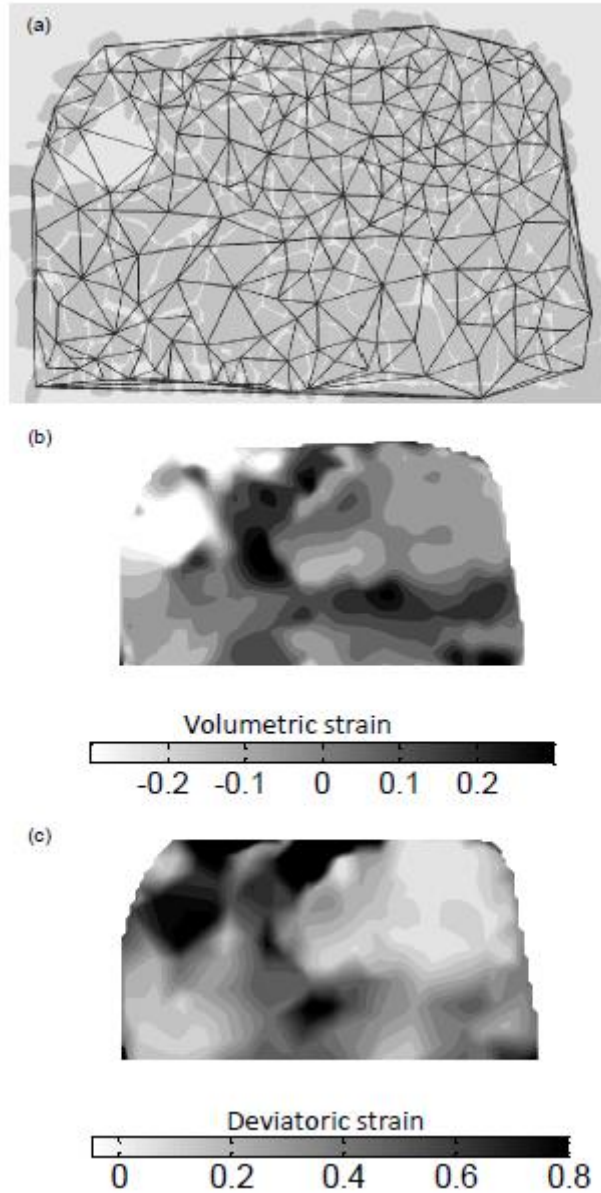
17

Figure 10: Analysis of the strains between stages 1 and 4 (a) Triangulation used for the calculations (b) Volumetric strain filed (positive values indicate dilation) (c) Deviatoric strain field.

In Figure 10(b) and (c), the greatest compaction, with values lower than -0.2, occurs in the region of the pore/surface sink as it is filled-in with the surrounding grains (Figure 3) and this region therefore undergoes a large shear strain. The remainder of the sample also has an inhomogeneous volumetric and shear strain field. A region of high shear and simultaneous dilation can be identified both vertically to the right of the large void and horizontally in the right-hand half of the field of view. Comparing with the grain level analysis, it can be confirmed that the regions of high shear and dilatational volumetric strain in Figure 10(b) – (c) correspond to regions of highest grain rotation (Figure 7b), the greatest reduction in

number of contacts per grain (Figure 5(d)), and the greatest increase in branch vector (Figure 6).

The heterogeneity of the strain fields in granular materials subject to macro-scale deformation, with some areas dilating and some areas contracting, has previously been observed in simulations [42] and experiments [43] on soils. Figure 11 is a plot of incremental volumetric strain against incremental deviatoric strain for each triangle in Figure 10a for each of the four stages considered. There is clearly, at a local level, volumetric strain associated with shear strain, further confirming that shear-induced volumetric strain occurs at both the grain level and the macroscopic level during the fully-fed deformation of carbon steels at 70-90% solid.
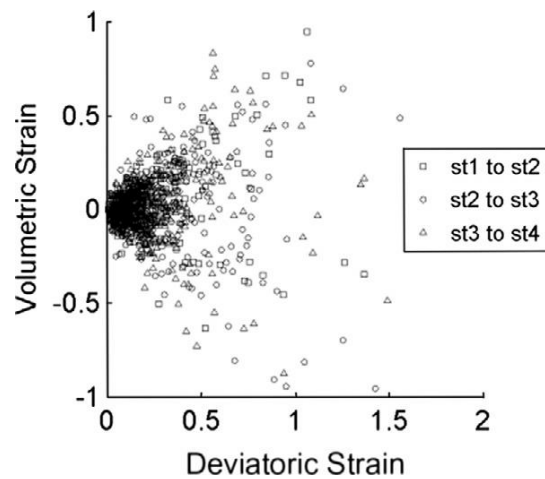

Figure 11: Incremental volumetric strains versus incremental deviatoric strains for triangular subregions illustrated in Figure 10(a) considering increments between the four deformation stages.

4   DISCUSSION

These experiments involved the near in-plane deformation of quasi-2-D grain assemblies, and have differences compared with bulk 3D deformation. For example, in a sample 0.4 median grain diameters thick, a much larger proportion of the contacts are with the confining walls than would be the case with bulk samples, and the shape of contacts will be different compared with fully-3D grains. There may be some loss of stress in the in-plane direction due to a frictional drag between the particles and the device wall, however this frictional loss will not influence the overall interpretation of mechanisms that is the

objective of this paper; no attempt is made to relate stresses and strains directly. Importantly, there is ample evidence in the soil mechanics literature of the benefits of using 2D analogues to real granular materials to gain insight into fundamental mechanisms that cannot be seen in the physical 3D material. Physical experiments using two-dimensional analogues (e.g. [44-46]) and numerical (DEM) studies in 2D (e.g. [33, 47]) have confirmed that, for granular materials, the overall responses of 2D systems are qualitatively similar to 3D systems; key phenomena such as the dependence of the material response on the stress level and void ratio, hysteresis, dilation upon shearing, etc. are all observed. The key measurements in this paper of the austenite grains rearranging as quasi-rigid bodies, transmitting shear and compressive forces across grain-grain contacts and causing shear-induced dilation, are basic granular phenomena that occur in both 2D and 3D. The results have confirmed that many of the fundamental grain-scale phenomena reported for granular materials, including soils, also occur in partially-solid steels at 70-90% solid.

In densely packed soils (including locked sands such as Fig. 2e-f), the grain assembly dilates under shear until a solid fraction is reached where grain rearrangement can occur at constant volume for the applied (constant) confining pressure. This solid fraction-loading combination is termed the critical state [48]. In the semi-solid steel studied here, the grain assembly dilated continually during the experiment (Figure 8(c)) and, therefore, did not reach the critical state. This is most likely because the plate displacement was only $3.1d_{50}$ for this geometry and larger displacements are required to bring the sample to the critical state. Further work at larger strains is required to confirm this.

Throughout this paper, the focus has been on the behaviour of the γ-Fe grains and the interstitial liquid has been largely ignored. This approach is suitable in the current study because, for the combination of a strain rate of 10^{-3} s^{-1}, ~80% solid and the presence of a liquid reservoir, deformation was fully-fed (i.e. liquid in-flow was able to accommodate the dilatancy without generating significant pressure gradients in the liquid). During this work, it was found that when similar experiments were conducted at ~80% solid without a liquid reservoir, shear-induced dilation caused the formation of defects (surface sinks, pores and cracks). These datasets will be analysed for a future publication. Furthermore, additional work is required to explore the microstructural response at higher strain rates where

restricted liquid flow will influence grain motion [12], encourage the formation of defects and, possibly, competition among deformation mechanisms.

Models of alloy deformation at high solid fraction (e.g. [4, 49]) usually assume that viscoplastic deformation of the solid is a significant component of deformation. However, it was found here that deformation at ~80% solid occurred by rearrangement of quasi-rigid grains without discernible grain deformation at the resolution of the experiment. We note that large deformations of individual grains have been reported at similar solid fractions (e.g.[1, 7]), and that the competition between the rearrangement of grains and the deformation of grains requires further investigation.

Grain rearrangement at ~80% solid caused shear-induced dilation. Most papers on semi-solid alloy deformation do not mention dilatancy (e.g. [1]) and most bulk mechanical tests commonly used on semi-solid alloys are not designed to measure volumetric strains. This paper shows that the altering packing-density of the grains is an important part of the microstructural response to load, and the work done in dilating the grain assembly against the confining pressure is, therefore, a significant contributor to shear strength in semi-solid alloys at high solid fraction (e.g. [50]). Furthermore, other materials that exhibit shear-induced dilation (densely-packed soils, powders etc.) exhibit pressure-dependent mechanics (i.e. yield criteria and flow laws that depend on the hydrostatic component of stress), suggesting that semi-solid alloys at high-solid fraction may well also be pressure-dependent.

The findings of this work therefore highlight the need to develop bulk mechanical tests for semi-solid alloys that can alter the confining pressure and measure volumetric strain, perhaps building on those in [22, 51], so that granular constitutive equations can be developed for semi-solid alloys. In soil mechanics, great care is taken to measure the volumetric strain, the liquid (i.e. pore fluid) pressure, and the degree of saturation with pore fluid (e.g. [52]). Since volumetric strains and liquid pressures are rarely measured in semi-solid alloys, only part of the rheological response is reported in most work on semi-solid alloys.

Recently, particulate numerical modelling including the discrete element method (DEM) has been applied to semi-solid alloy deformation [10, 53, 54]. The grain-level similarities between semi-solid metals and granular materials including soils measured in this work

confirm that DEM is a suitable approach to simulating the response of semi-solid metals under loading.

Conclusions

Quantitative image analysis of high resolution radiographs of the deformation of semi-solid steel at ~80% solid has confirmed the tendency of this semi-solid material to behave as a granular material. In particular the data have shown that the grains rearrange as quasi-rigid particles and that the grain assembly as a whole dilates during shear. These observations support the hypothesis that the behaviour of semi-solid steel can be interpreted using the frameworks developed for soil, e.g. critical state soil mechanics [55]. A natural sand, Reigate sand, was identified as having characteristics that were particularly similar to this semi-solid alloy microstructure and the similarities in the behaviour of the two materials were identified at both the macro- and grain-scales.

This study suggests that new approaches to testing the mechanical response of semi-solid metals should be developed taking inspiration from soil mechanics testing apparatus. In particular, the measurement of volumetric strains and liquid pressures should be given greater consideration in experimental semi-solid metallurgy. The results also support the use of particulate numerical modelling (e.g. DEM) for mushy-zone deformation.

Appendix A. Supplementary material

Supplementary data associated with this article can be found, in the online version, at http://dx.doi.org/10.1016/j.actamat.2013.03.043.

References

1. Flemings, M.C., *Behavior of Metal Alloys in the Semisolid State.* Metallurgical Transactions A, 1991. **22**(3): p. 957-976.
2. Rassili, A. and H.V. Atkinson, *A review on steel thixoforming.* Transactions of Nonferrous Metals Society of China, 2010. **20**: p. S1048-S1054.
3. Eskin, D.G., Suyitno, and L. Katgerman, *Mechanical properties in the semi-solid state and hot tearing of aluminium alloys.* Progress in Materials Science, 2004. **49**(5): p. 629-711.
4. Ludwig, O., et al., *Rheological behavior of Al-Cu alloys during solidification: Constitutive modeling, experimental identification, and numerical study.* Metallurgical and Materials Transactions A, 2005. **36A**(6): p. 1525-1535.
5. Young, K.P., R.G. Riek, and M.C. Flemings, *Structure and Properties of Thixocast Steels.* Metals Technology, 1979. **6**(APR): p. 130-137.
6. Joly, P.A. and R. Mehrabian, *The rheology of a partially solid alloy.* Journal of Materials Science, 1976. **11**: p. 1393-1418.
7. Suéry, M. and M.C. Flemings, *Effect of strain rate on deformation-behavior of semisolid dendritic alloys.* Metallurgical Transactions A, 1982. **13**(10): p. 1809-1819.
8. Chen, C.P. and C.-Y. Tsao, *Semi-solid deformation of non-dendritic structures- I Phenomenological Behaviour.* Acta Materialia, 1997. **45**(5): p. 1955-1968.
9. Gourlay, C.M., B. Meylan, and A.K. Dahle, *Shear mechanisms at 0-50% solid during equiaxed dendritic solidification of an AZ91 magnesium alloy.* Acta Materialia, 2008. **56**: p. 3403-3413.
10. Vernède, S., P. Jarry, and M. Rappaz, *A granular model of equiaxed mushy zones: Formation of a coherent solid and localization of feeding.* Acta Materialia, 2006. **54**(15): p. 4023-4034.
11. Gourlay, C.M. and A.K. Dahle, *Dilatant shear bands in solidifying metals.* Nature, 2007. **445**: p. 70-73.
12. Vernède, S., J.A. Dantzig, and M. Rappaz, *A mesoscale granular model for the mechanical behavior of alloys during solidification.* Acta Materialia, 2009. **57**(5): p. 1554-1569.
13. Gourlay, C.M., et al., *Granular deformation mechanisms in semi-solid alloys.* Acta Materialia, 2011. **59**(12): p. 4933–4943.
14. Phillion, A.B., et al., *In situ X-ray observation of semi-solid deformation and failure in Al-Cu alloys.* Acta Materialia, 2011. **59**(4): p. 1436-1444.
15. Terzi, S., et al., *In situ X-ray tomography observation of inhomogeneous deformation in semi-solid aluminium alloys.* Scripta Materialia, 2009. **61**(5): p. 449-452.
16. Zabler, S., et al., *Particle and liquid motion in semi-solid aluminium alloys: A quantitative in situ microradioscopy study.* Acta Materialia, 2013. **61**: p. 1244–1253.
17. Kareh, K.M., P.D. Lee, and C.M. Gourlay, *In situ, time-resolved tomography for validating models of deformation in semi-solid alloys*, in *MCWASP Xiii: International Conference on Modeling of Casting, Welding and Advanced Solidification Processes*, A. Ludwig, Editor 2012.
18. Nagira, T., et al., *Direct observation of deformation in semi-solid carbon steel.* Scripta Materialia, 2011. **64**(12): p. 1129-1132.
19. Jaeger, H.M. and S.R. Nagel, *Physics of the granular state.* Science, 1992. **255**: p. 1523-1531.
20. Reynolds, O., *On the dilatancy of media composed of rigid particles in contact.* Philosphical Magazine, 1885. **20**(127): p. 469-481.
21. Casagrande, A., *Characteristics of cohesionless soils affecting the stability of slopes and earth fills.* Journal of the Boston Society of Civil Engineers, 1936. **23**(1): p. 13-32.
22. Meylan, B., et al., *Dilatancy and rheology at 0–60% solid during equiaxed solidification.* Acta Materialia, 2011. **59**: p. 3091-3101.
23. Mitchell, J.K. and K. Soga, *Fundamentals of soil behavior* 2005, Hoboken, NJ John Wiley & Sons.
24. Been, K. and M.G. Jefferies, *A state parameter for sands.* Géotechnique, 1985. **35**(2): p. 99–112.

25. Tatsuoka, F., *Strength and dilatancy of sands: Discussion.* Géotechnique, 1987. **37**(2): p. 219-225.
26. Yasuda, H., et al., *Development of X-ray Imaging for Observing Solidification of Carbon Steels.* ISIJ International, 2011. **51**(3): p. 402-408.
27. Goto, S., et al., *Construction and commissioning of a 215-m-long beamline at SPring-8.* Nuclear Instruments & Methods in Physics Research A, 2001. **467**: p. 682-685.
28. Lings, M.L. and M.S. Dietz, *An improved direct shear apparatus for sand.* Geotechnique, 2004. **54**(4): p. 245-256.
29. Sumitomo, T., D.H. StJohn, and T. Steinberg, *The shear behaviour of partially solidified Al-Si-Cu alloys.* Materials Science and Engineering A, 2000. **289**(1-2): p. 18-29.
30. Wang, H., et al., *Characterization and shear behaviour of semisolid Al-7Si-0.35Mg alloy microstructures.* Aluminum Transactions, 2000. **2**(1): p. 57-66.
31. Robertson, P.K., *Soil classification using the cone penetration test.* Canadian Geotechnical Journal, 1990. **27**(1): p. 151-158.
32. Cui, L. and C. O'Sullivan, *Exploring the macro- and micro-scale response of an idealised granular material in the direct shear apparatus.* Géotechnique, 2006. **56**(7): p. 455-468.
33. Wang, J. and M. Gutierrez, *Discrete element simulations of direct shear specimen scale effects.* Géotechnique, 2010. **60**(5): p. 395-409.
34. Fonseca, J., *The evolution of morphology and fabric of a sand during shearing*, 2011, Imperial College London, University of London.
35. Barton, M., ed. *Cohesive sands: The natural transition from sands to sandstones.* Geotechnical Engineering of Hard Soils-Soft Rocks, ed. Anagnostopoulos1993: Rotterdam, The Netherlands.
36. Fonseca, J., et al., *Quantifying the Evolution of Soil Fabric during Shearing using Directional Parameters.* Géotechnique 2012. ***in press***.
37. Cresswell, A. and W. Powrie, *Triaxial tests on an unbonded locked sand.* Géotechnique, 2004. **54**(2): p. 107-115.
38. Wang, L.B., J.D. Frost, and J.S. Lai, *Quantification of doublet vector distribution of granular materials.* Journal of Engineering Mechanics, 2001. **127**(7): p. 720-729.
39. Bathurst, R.J. and L. Rothenburg, *Observations on stress-force-fabric relationships in idealized granular materials.* Mechanics of Materials, 1990. **9**(1): p. 65-80.
40. Haralik, R. and L. Shapiro, *Computer and Robot Vision* 1992: Addison Wesley Longman Publishing Co.
41. Marketos, G. and M.D. Bolton, *Flat boundaries and their effect on sand testing.* International Journal for Numerical and Analytical Methods in Geomechanics, 2010. **34**(8): p. 821-837.
42. O'Sullivan, C., J.D. Bray, and S.F. Li, *A new approach for calculating strain for particulate media.* International Journal for Numerical and Analytical Methods in Geomechanics, 2003. **27**: p. 859-877.
43. Rechenmacher, A., S. Abedi, and O. Chupin, *Evolution of force chains in shear bands in sands.* Geotechnique, 2010. **60**(5): p. 343-351.
44. de Josselin de Jong, G. and A. Verrujit, *Etude photoelastique d'un empilement de disques.* Cahiers du Groupe Français de Rheologie II, 1969: p. 73-86.
45. Oda, M., S. Nemat-Nasser, and J. Konishi, *Stress-induced anisotropy in granular masses.* Soils and Foundations, 1985. **25**(3): p. 85-97.
46. Ibraim, E., et al., *Strain path controlled shear tests on an analogue granular material.* Géotechnique, 2010. **60**(7): p. 545-559.
47. Rothenburg, L. and R.J. Bathurst, *Analytical study of of induced anisotropy in idealized granular materials.* Géotechnique, 1989. **39**(4): p. 601-614.
48. Roscoe, K.H., *On the yielding of soils.* Géotechnique, 1958. **8**(1): p. 22.

49.   Zavaliangos, A., *Modeling of the mechanical behaviour of semisolid metallic alloys at high volume fractions of solid.* International Journal of Mechanical Sciences, 1998. **40**(10): p. 1029-1041.

50.   Bolton, M.D., *The strength and dilatancy of sands.* Geotechnique, 1986. **36**(1): p. 65-78.

51.   Nguyen, T.G., D. Favier, and M. Suéry, *Theoretical and experimental study of the isothermal mechanical behaviour of alloys in the semi-solid state.* International Journal of Plasticity, 1994. **10**(6): p. 663-693.

52.   Head, K.H., *Manual of Soil Laboratory Testing: Effective Stress Tests Vol 3* Vol. 3. 1997: Wiley.

53.   Sistaninia, M., et al., *Simulation of Semi-Solid Material Mechanical Behavior Using a Combined Discrete/Finite Element Method.* Metallurgical and Materials Transactions A, 2011. **42A**(1): p. 239-248.

54.   Yuan, L., C. O'Sullivan, and C.M. Gourlay, *Exploring dendrite coherency with the discrete element method.* Acta Materialia, 2012. **60**(3): p. 1334-1345.

55.   Schofield, A. and C. Wroth, *Critical State Soil Mechanics*1968: McGraw Hill.